

Article

Orientation-Mediated Luminescence Enhancement and Spin-Orbit Coupling in ZnO Single Crystals

Ali Hassan ^{1,2,*}, Abbas Ahmad Khan ^{3,*}, Yeong Hwan Ahn ³, Muhammad Azam ⁴, Muhammad Zubair ⁵, Wei Xue ^{1,6} and Yu Cao ^{1,6,*}

¹ China International Science & Technology Cooperation Base for Laser Processing Robotics, Wenzhou University, Wenzhou 325035, China; xm@wzu.edu.cn

² Zhejiang Provincial Key Laboratory of Laser Processing Robotics, College of Mechanical and Electrical Engineering, Wenzhou University, Wenzhou 325035, China

³ Department of Physics and Department of Energy Systems Research, Ajou University, Suwon 16499, Korea; ahny@ajou.ac.kr

⁴ Department of Physics, Faculty of Sciences, University of Central Punjab, Lahore 54000, Pakistan; muhammad.azam01@ucp.edu.pk

⁵ Centre for Advanced Materials Application CEMEA, Slovak Academy of Sciences, Dubravská Cesta 9, 845 11 Bratislava, Slovakia; muhammad.zubair@savba.sk

⁶ Oujiang Laboratory (Zhejiang Lab for Regenerative Medicine, Vision and Brain Health), Wenzhou University, Wenzhou 325000, China

* Correspondence: alirao@wzu.edu.cn (A.H.); abbaskhan@ajou.ac.kr (A.A.K.); yucao@wzu.edu.cn (Y.C.)



Citation: Hassan, A.; Khan, A.A.; Ahn, Y.H.; Azam, M.; Zubair, M.; Xue, W.; Cao, Y. Orientation-Mediated Luminescence Enhancement and Spin-Orbit Coupling in ZnO Single Crystals. *Nanomaterials* **2022**, *12*, 2192. <https://doi.org/10.3390/nano12132192>

Academic Editors: Vladimir Falko and Jin-Cherng Hsu

Received: 25 May 2022

Accepted: 23 June 2022

Published: 26 June 2022

Publisher's Note: MDPI stays neutral with regard to jurisdictional claims in published maps and institutional affiliations.



Copyright: © 2022 by the authors. Licensee MDPI, Basel, Switzerland. This article is an open access article distributed under the terms and conditions of the Creative Commons Attribution (CC BY) license (<https://creativecommons.org/licenses/by/4.0/>).

Abstract: Temperature-, excitation wavelength-, and excitation power-dependent photoluminescence (PL) spectroscopy have been utilized to investigate the orientation-modulated near band edge emission (NBE) and deep level emission (DLE) of ZnO single crystals (SCs). The near-band-edge emission of ZnO SC with $<0001>$ orientation exhibits strong and sharp emission intensity with suppressed deep level defects (mostly caused by oxygen vacancies V_O). Furthermore, Raman analysis reveals that $<0001>$ orientation has dominant E_2 (high) and E_2 (low) modes, indicating that this direction has better crystallinity. At low temperature, the neutral donor-to-bound exciton (D^0X) transition dominates, regardless of the orientation, according to the temperature-dependent PL spectra. Moreover, free-exciton (FX) transition emerges at higher temperatures in all orientations. The PL intensity dependence on the excitation power has been described in terms of power-law ($I \sim L^\alpha$). Our results demonstrate that the α for $<0001>$, $<1120>$, and $<1010>$ is (1.148), (1.180), and (1.184) respectively. In short, the comprehensive PL analysis suggests that D^0X transitions are dominant in the NBE region, whereas oxygen vacancies (V_O) are the dominant deep levels in ZnO. In addition, the $<0001>$ orientation contains fewer V_O -related defects with intense excitonic emission in the near band edge region than other counterparts, even at high temperature (~543 K). These results indicate that $<0001>$ growth direction is favorable for fabricating ZnO-based highly efficient optoelectronic devices.

Keywords: zinc oxide; single crystal; photoluminescence; exciton; impurities and defects

1. Introduction

Single crystals, especially from metal oxides, received enormous attention worldwide in the past few decades due to their distinguished optoelectronic and gas sensing properties over a large scale [1–4]. Single crystals of zinc oxide, a wide and direct bandgap (~3.37 eV) semiconductor, gained extra interest among other counterparts due to its unique luminescence feature at 378 nm wavelength and large exciton binding energy (60 meV) [5–7]. The intense near band edge emission and the large exciton binding energy make ZnO a promising candidate for optoelectronic devices such as laser diodes [8], light-emitting diodes [9], and photodetectors [10]. Moreover, the availability of polar and non-polar faces in zinc oxide single crystal adds variety in tuning its optical and electronic properties;

for example, radiation absorption and emission from ultraviolet (UV) to near-infrared (NIR) region [11,12]. To achieve the best output from ZnO-based devices, it is important to select a suitable growth direction (polar and non-polar faces) depending upon own needs. For instance, Sasaki et al. [13] recently observed the large densities of surface states in O-faced ZnO single crystal which cause trap electrons near these surfaces and activate the ionized donor bound exciton (D^+X) [14]. However, their results proposed that the Zn-faced single crystal has fewer surface states of ionized impurities, which results in the absence of an ionized donor bound exciton (D^+X) peak. It is essential to control the non-recombination centers present in the single crystal to gain high device efficiency with low defect concentration [15–17].

The choice of different orientations depends on the desired property. Mostly, $<0001>$ orientation has been found to be good for the growth of high UV emission ZnO-based devices (UV detectors or UV lasers). Recently, Jacobs et al. [18] reported the high near band edge emission with completely suppressed deep level defect luminescence in polar ZnO-based heterojunction light emitting diodes (LEDs). The suppression of deep levels enhances the device stability over a longer time and minimizes the heating effects produced by phonon vibrations. Valtiner et al. [3] examined the photo-corrosion mechanism of polar $<0001>$ and non-polar $<1010>$ ZnO single crystals. Their study shows the ideal stability at very low potential and under hydrogen evolution conditions on polar $<0001>$ surface. In contrast, the non-polar $<1010>$ surface was inactive for water splitting and sustained a higher degree of dissolution. Despite the considerable impact of polar and non-polar surfaces of ZnO single crystals on the modulation of luminescence and sensing properties, it has been noted that there are few reports presented in the literature to discuss their orientation-dependent photoluminescence mechanism; at room temperature as well as at low temperature [13,19,20].

Considering the above-mentioned facts, the present work is completely devoted to the understanding of luminescence mechanism and presence of different emission bands in polar $<0001>$ and non-polar $<1120>$, $<1010>$ ZnO single crystals from high temperature to low-temperature (543–123 K). Moreover, the effect of different excitation power on near band edge and deep level emission sites has also been discussed systematically. The current study will help to cognize the more detailed phenomena of luminescence characteristics and defect emission in different polar and non-polar ZnO single crystals, which will further pave the way to building more efficient optoelectronic devices. Despite having excellent photoelectric properties, the practical applications of ZnO-based optoelectronic devices have been restricted due to the unavailability of a defect-free homoepitaxial substrate that can minimize the lattice mismatches and ion diffusion offered by foreign substrates. Therefore, the current study proposed that the use of $<0001>$ ZnO single crystal can solve the problem of lattice mismatch and ionic diffusion offered by a heteroepitaxial substrate. Furthermore, the heat mismatching or phonon generation can also be suppressed by the utilization of $<0001>$ single crystal as a homoepitaxial substrate in ZnO-based optoelectronic devices.

2. Materials and Methods

Hydrothermally grown as prepared ZnO single crystals, having dimensions $10 \times 10 \times 5 \text{ mm}^3$ with three different orientations ($<0001>$, $<1120>$, $<1010>$) were purchased from (HF-Kejing, Hefei, China). An Andor 550 spectrometer (Oxford Instruments, Abingdon, UK) with two excitation wavelengths (320 nm, 405 nm) was employed to measure the micro-PL combined with a Newton 920 CCD detector (Oxford Instruments, Abingdon, United Kingdom). Micro-Raman for ZnO single crystals was measured using 405 nm and 532 nm wavelength in a backscattering mode of LAB Raman HR Raman spectrometer (Horiba Scientific, Kyoto, Japan). The excitation laser was focused on the sample using a confocal microscope having a $50\times$ objective lens with a 5-micrometer spot size for 320 nm and 1-micrometer for 532 nm excitation wavelength. Here, it is worth mentioning that the spot size does not depend on the pump power of the excitation laser under confocal

microscopic conditions. The X-ray diffraction (Rigaku D/MAX-2004 from Rigaku Corporation, Tokyo, Japan) was applied to characterize the structural analysis of single crystals. Field-emission electron microscopy (FESEM) (model Hitachi S-4800 from Hitachi, Ltd. Tokyo, Japan) equipped with the *in situ* energy dispersive X-ray spectroscopy (EDS) was implanted to check the morphology and elemental composition. X-ray photoelectron spectroscopy (XPS) from ThermoFisher Scientific, Waltham, MA, USA, model; Thermo Scientific K-Alpha was utilized to study the chemical bonding and core-level mapping of ZnO single crystals. The excitation source was Al K α having photon energy of 1486.6 eV with a beam spot of 400 μ m. The chamber pressure was kept 5×10^{-7} mBar with a working voltage of 12 kV and filament current of 6 mA. The conduction energy for core-level spectra was kept 50 eV with a step length of 0.1 eV. The binding energy of C 1 s (284.80 eV) was taken as a reference for this work. The atomic force microscopy (AFM) model (Bruker Dimension Icon, from Bruker Corporation, Billerica, MA, USA) has been used in tapping mode for surface topography and surface roughness study of single crystals.

3. Results and Discussions

3.1. Surface Morphology, X-ray Diffraction, and Raman Analysis

Figure 1a shows the smooth surface of as-received ZnO single crystals without any surface contamination (surface smoothness further verified via atomic force microscopic 2D image shown in Figure 4 discussed later). Moreover, the elemental analysis was carried out to check the sample's elemental composition and it was found that the single crystals are Zn-rich with slightly high atomic percentage (at%, Zn~57.05, O~42.95) as shown in Figure 1b, c. Here, it is worth noting that the measured atomic percentage has been carried out by energy dispersive X-ray spectroscopy (EDS) which does not provide the elemental composition about whole single crystal as it only detects the surface. Moreover, the accuracy of EDS is affected by several other factors, including but not limited to the overlapping X-rays emission peaks, sample nature, and the X-ray escaping from the sample which did not reach the detector. The XRD graph (Figure 1d) exhibits that all three samples are grown in different preferential directions without any impurity peak. However, the <1010> orientation contains an additional peak (0002) at 2 θ (34.3), which belongs to the <0001> orientation. It suggests that <1010> orientation of ZnO single crystal is not so stable. Franks et al. [11] also proposed that the <1010> orientation is unstable due to the higher surface O atoms attached per Zn tetrahedron. The peak (2020) is another crystallographic plane of <1010> orientation according to the JCPDS: 36-1451 of zinc oxide. The higher surface oxygen atoms in the <1010> can imbalance the stability of the <1010> orientation, which can cause the lattice mismatch in the <1010> orientation and some atoms which lie in the (0002) plane shows XRD reflection. Figure 1e,f shows the orientation-dependent Raman spectra measured at room temperature with two different excitation wavelengths. We have identified several characteristics vibrational modes for ZnO single crystals using 532 nm excitation wavelength, which corresponds to E₂(low), E₂(high)-E₂(low), A₁(TO), E₂(high), AM, 2A₁(LO)+E₁(LO), and 2LO. However, the observed vibrational modes using 405 nm excitation wavelength are E₂(high)-E₂(low), E₁(TO), E₂(high), AM, and A₁(2LO), respectively. Table 1 represents the corresponding wavenumbers associated with each Raman mode. It has been well noted that the ZnO single crystal contains a wurtzite structure that belongs to the P6₃mc space group. The four atoms in the unit cell result in twelve phonon modes, of which nine are optical, and three are acoustic. The nine optical modes are further divided into the A₁ branch, one double degenerate E₁ branch, two double degenerate E₂ branches, and two inactive B₁ branches [21,22]. Here, A₁ and E₁ are predicted as the polar modes and further split into longitudinal optical (LO) and transverse optical (TO) phonons, respectively. The E₂ mode contains the E₂(high) and E₂(low) optical modes; E₂(high) mode arises as a result of vibration generated by the oxygen atom. On the other hand, E₂(low) mode appears due to the vibration originated by the Zn sublattice [23].

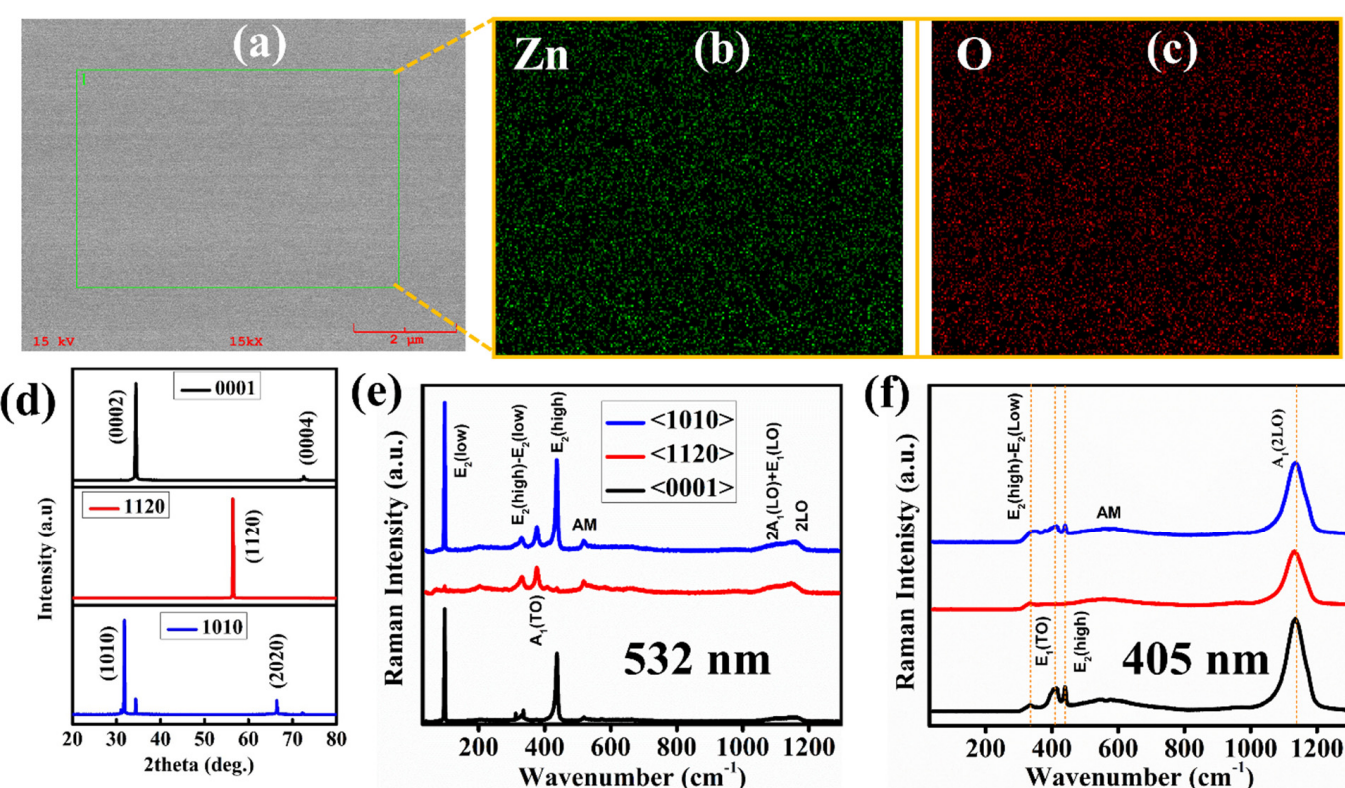


Figure 1. (a–c) Field-emission electron microscopy (FE-SEM) and energy dispersive spectroscopy (EDS) image of <0001> single crystal (d) XRD micrographs of all three ZnO single crystals <0001>, <1120> and <1010>. The Raman spectra of ZnO single crystals were measured with (e) an excitation wavelength of 532 nm and (f) 405 nm.

Table 1. Summary of Raman vibrational modes in the literature and observed in current study for ZnO single crystals with polar and non-polar faces.

Sr#	Raman Shift (cm^{-1}) of ZnO Single Crystals Measured in the Current Study	Raman Shift (cm^{-1}) of ZnO Single Crystals Reported in the Literature [24,25]	Peak Identity	Symmetry
1	97	99	E ₂ (low)	E ₂ (Brillouin zone Γ)
2	331	333	E ₂ (high)–E ₂ (low)	E ₂ , E ₁ (Brillouin zone Γ)
3	375	379	A ₁ (TO)	A ₁ (Brillouin zone Γ)
4	435	438	E ₂ (high)	E ₂ (Brillouin zone Γ)
5	518		AM	-
6	1097	1102	2A ₁ (LO) + E ₁ (LO)	A ₁ , E ₁
7	1136	1138	A ₁ , 2LO	-
8	1159	1154	2LO	Wurtzite ZnO, 2LO

Figure 1e shows that in <0001> and <1010>, the E₂(low) and E₂(high) modes are prominent, whereas in <1120> orientation, these modes are very weak, and A₁(TO) is prominent. The appearance of A₁(TO) is usually attributed to the oxygen vacancies or Zn interstitials or their complexes [24], this indicates that the oxygen vacancies or Zn interstitials are higher in this orientation. No shift has been observed in the main characteristic Raman peaks in all three orientations, which indicates that all single crystals are free from extrinsic defects or impurities. The only defects in these single crystals are intrinsic defects,

which are either oxygen vacancies or Zn interstitials. Furthermore, the absence of $A_1(TO)$ in the $\langle 0001 \rangle$ orientation may be explained in terms of phonon Raman scattering intensity using lattice dynamics theory, which states that if the incident light is perpendicular to the $\langle 0001 \rangle$ direction, the $A_1(TO)$ vibration will not emerge. Figure 1f presents the Raman spectra of ZnO single crystals with different orientations measured at room temperature with 405 nm excitation wavelength. It has been discovered that regardless of the orientation, the excitation wavelength significantly impacts the vibrational characteristics of ZnO single crystals. It is clear that the dominating vibrational modes have shifted nominally when utilizing a 405 nm excitation wavelength. All three orientations contain the $A_1(2LO)$ dominant Raman modes with high intensity compared to other modes. The discovery of this phenomenon implies that changing the excitation wavelength produces precise energy that is necessary to activate specific modes. The electron-phonon coupling becomes robust when the excitation wavelength is comparable to the energy required to activate that specific Raman mode. For example, excitation at 405 nm provides enough energy to populate the transition from the $A_1(2LO)$ site. The 532 nm excitation, on the other hand, provides sufficient energy to ignite the optical transition from E_2 modes. Furthermore, Cardona et al. proposed that if the excitation wavelength is just below the bandgap, the scattering efficiency of the 2LO process can be improved due to resonant events [26].

3.2. X-ray Photoelectron Spectroscopy Measurement

X-ray photoelectron spectroscopy (XPS) measurements were used to explore the bonding nature and chemical states of Zn and O atoms in single crystals. Figure 2a shows the Zn 2p core-level spectra of polar and non-polar ZnO single crystals. The binding energies of Zn 2p_{3/2} and Zn 2p_{1/2} peaks were observed at 1020.70 eV and 1043.78 eV for $\langle 0001 \rangle$, 1020.62 eV and 1043.70 eV for $\langle 1010 \rangle$, 1020.59 eV and 1043.67 eV for $\langle 1120 \rangle$ orientation, respectively. Spin-orbit splitting of $\Delta E \sim 23.08$ eV has been observed for all three samples, confirming that Zn's chemical valence state at the surface of all three single crystals is Zn²⁺ oxidation state [27,28]. Moreover, a negative shift of 0.08 eV for $\langle 1010 \rangle$ and 0.11 eV for $\langle 1120 \rangle$ orientation has been observed in the binding energies of Zn 2p core-level spectra, which indicates that the majority of Zn atoms in the tetrahedral wurtzite geometry are in Zn²⁺ oxidation state. However, the presence of Zn_i and V_{Zn} cannot be ruled out [29]. Furthermore, a shift to the lower binding energy of Zn 2p_{3/2} for $\langle 1010 \rangle$ and $\langle 1120 \rangle$ orientations indicates that the oxygen vacancies present within the bulk crystal lattice dominate and could be a reason for green luminescence in ZnO (discussed in room-temperature PL section). The normalized core-level spectra of O 1 s for ZnO single crystals with three distinct orientations are shown in Figure 2b. The asymmetric structure of the O 1 s peak is due to the presence of different oxygen coordination in all three orientations [30]. To get a better qualitative analysis of different oxygen coordination and their concentration, we deconvoluted the O 1 s spectra using the Gaussian fitting function (Figure 2c–e). The three Gaussian peaks at $\sim 529.86 \pm 0.12$ eV (Peak 1), $\sim 531.28 \pm 0.12$ eV (Peak 2), and 532.61 ± 0.12 eV (Peak 3) were observed in all three orientations of the ZnO single crystal. All peaks show a shift toward high binding energy in non-polar orientation, which could be attributed to the surface oxygen vacancies of ZnO as observed by Tay et al. [29]. Here, peak-1 represents the O²⁻ ions in Zn-O bonding of the wurtzite structure of ZnO, peak-2 attributed to the oxygen vacancies within the crystal lattice of ZnO, whereas peak-3 denotes the loosely bounded oxygen atoms on the surface of ZnO single crystals, which belongs to some specific species like adsorbed O₂ and H₂O, or –CO₃ [31]. We integrated the total area of O 1 s peak and the ratio of each deconvoluted peak and found that the ratio of peak-1 and peak-2 in $\langle 1010 \rangle$ and $\langle 1120 \rangle$ is higher than that of $\langle 0001 \rangle$ orientation, which indicates that the oxygen vacancies/defects and O²⁺ ions within the crystal lattice in these two orientations are present in excess. XPS core-level mapping of Zn 2p and O 1 s (Figure 3a,b) also confirms that the oxygen-related defects at the surface of $\langle 1010 \rangle$ and $\langle 1120 \rangle$ non-polar ZnO single crystal are quite high as compared to the polar $\langle 0001 \rangle$ ZnO single crystal.

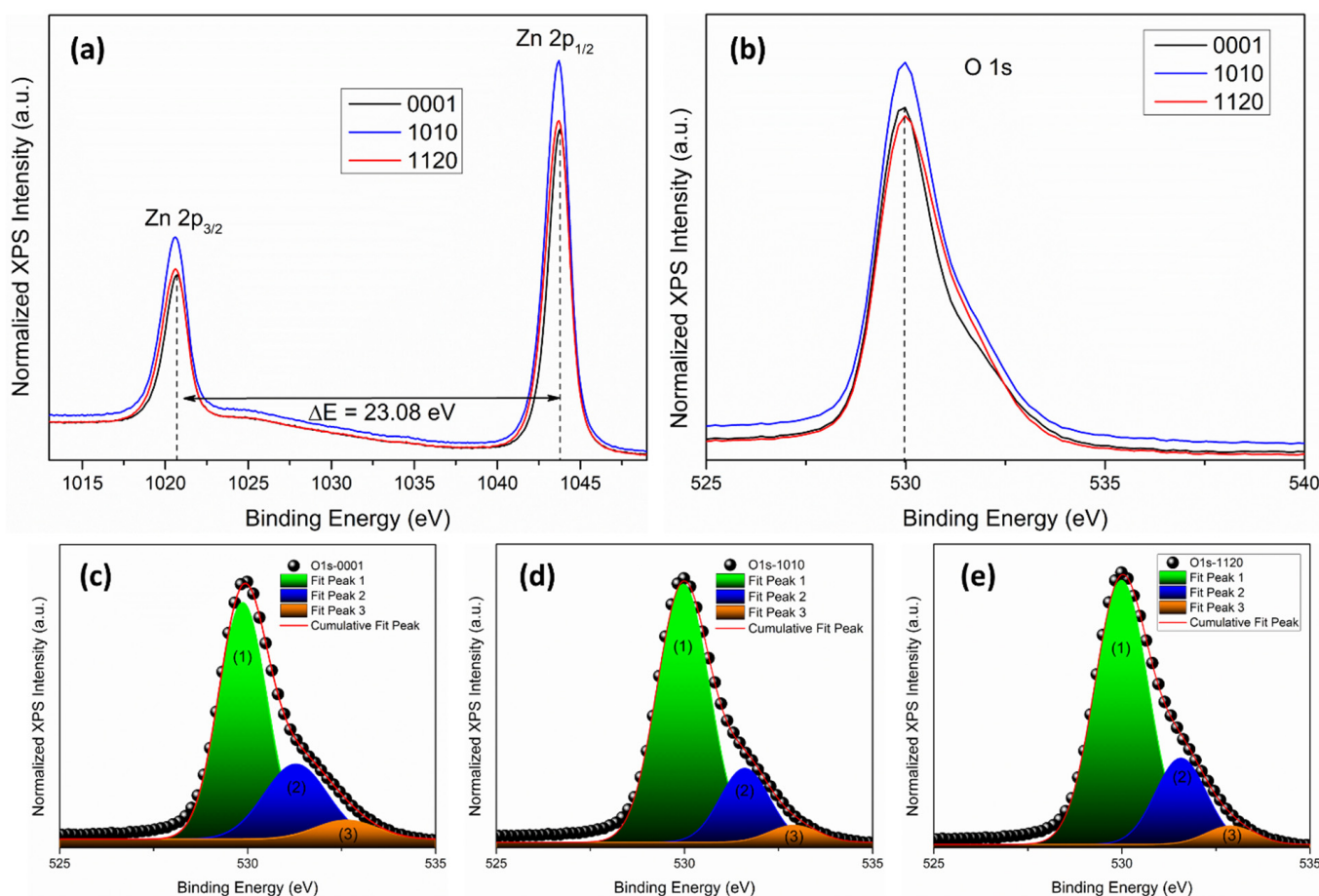


Figure 2. XPS core-level spectra of (a) Zn 2p and (b) O 1 s. The black dashed line indicates the peak position, and the horizontal double-head arrow represents the spin-orbit splitting ($\Delta E = 23.08 \text{ eV}$). Deconvoluted features of the O 1 s peak for (c) $<0001>$, (d) $<1010>$, and (e) $<1120>$ orientation. Black spheres represent experimental values, and the continuous red line indicates fitted results using the Gaussian fitting function.

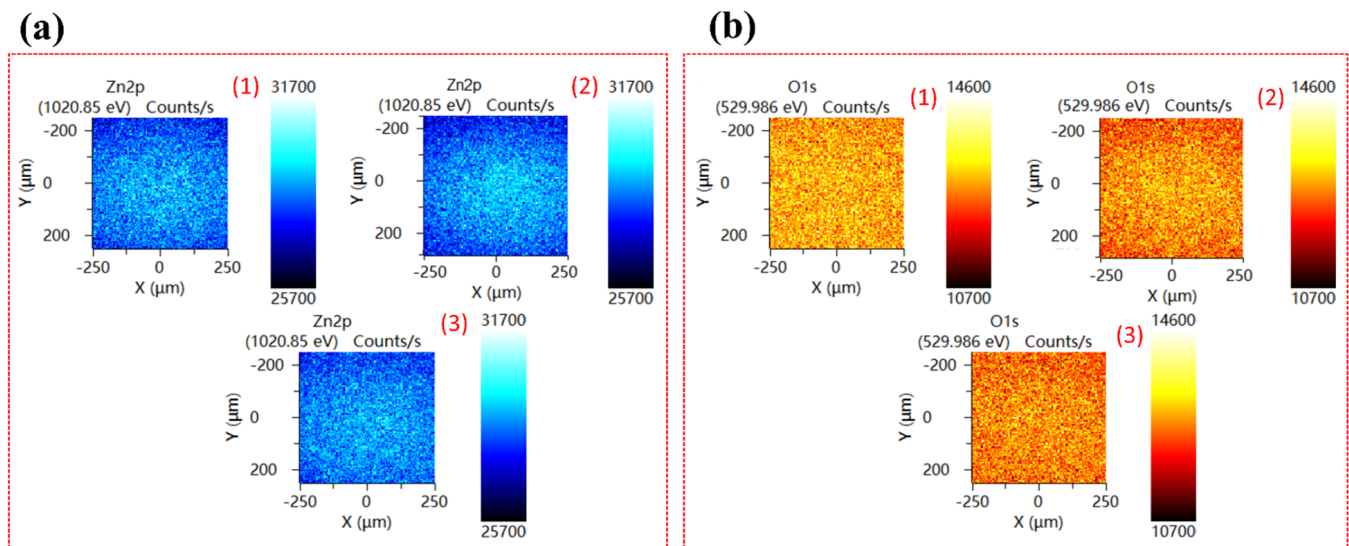


Figure 3. XPS core-level mapping of (a) Zn 2p and (b) O 1s ZnO single crystals; with polar (1) $<0001>$, and non-polar (2) $<1010>$, (3) $<1120>$ orientations.

3.3. Atomic Force Microscopy Analysis

To deeply investigate the surface morphology and roughness of ZnO single crystals, atomic force microscopic (AFM) analysis in tapping mode has been performed, as shown in Figure 4a–c. The 2D micrographs indicate that surface of all three single crystals is relatively smooth with a surface roughness ranging from 0.214 nm to 0.277 nm and with a height (Z) sensor noise level or error of 0.035 nm, while a few cracks (white dashed lines) occur at the surface of <1010> and <1120> non-polar orientation which could be formed after synthesis and can be neglected. These results indicate that the morphology-related effects (grain size and shape) are not dominant in modulating the optoelectronic properties of ZnO single crystals in the present situation. Moreover, it is well-known that the shape and size of grain have an insignificant dependence on the polarity of a single crystal, if there is no substantial doping or post-treatment effect taken place. In contrast, the preparation route, post-annealing treatment, and doping can tailor the shape and size of grain and consequently modulate the surface roughness [32,33].

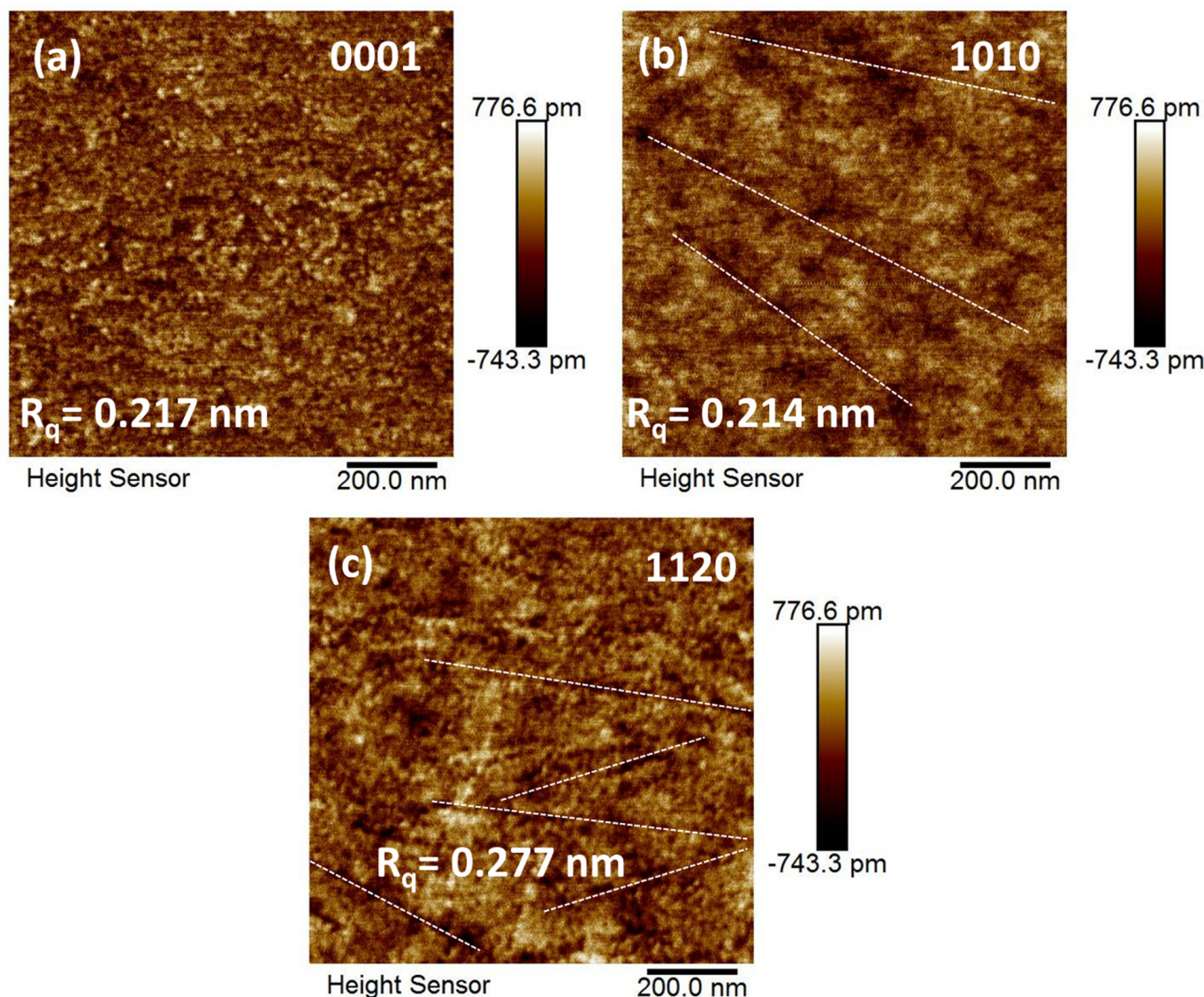


Figure 4. Two-dimensional AFM images of polar (a) $<0001>$ and non-polar (b) $<1010>$, (c) $<1120>$ ZnO single crystals. The white dashed line indicates the nano-scale cracks on the surface of single crystals. The surface roughness value of each single crystal surface was measured with a minimal standard deviation of 0.035 nm.

3.4. Room-Temperature and Low-Temperature Photoluminescence Spectroscopy

The room-temperature (300 K) photoluminescence measurements have been performed to examine the various emissions sites (from near band edge to deep levels emission) dependency on the orientation of single crystals. Figure 5a,b shows that the highest near band edge emission with low emission from deep levels has been obtained from <0001> sample when the samples were excited with the excitation wavelength 320 nm, and the other two SCs gave very low emission from near band edge and high emission from deep levels. Even the excitation wavelength is comparable with the bandgap of the ZnO but different intensity from different orientation points that the emission sites concentration varies as we change the orientation. The presence of high NBE emission in <0001> face with weak emission in DLE region states that, in <0001> the electron-hole recombination is dominant and the vacancies level is lower in this orientation as we know that the deep level emission is mainly attributed to various intrinsic defects as shown in Figure 6 (such as V_{Zn} , V_O , Zn_i , and O_i) [34–36]. Generally, in intrinsic ZnO, V_o and Zn_i are two notable defects that act as deep and shallow defects, respectively [37]. The difference in defect-luminescence from ZnO with different orientations can be described based on the formation energies of these defects.

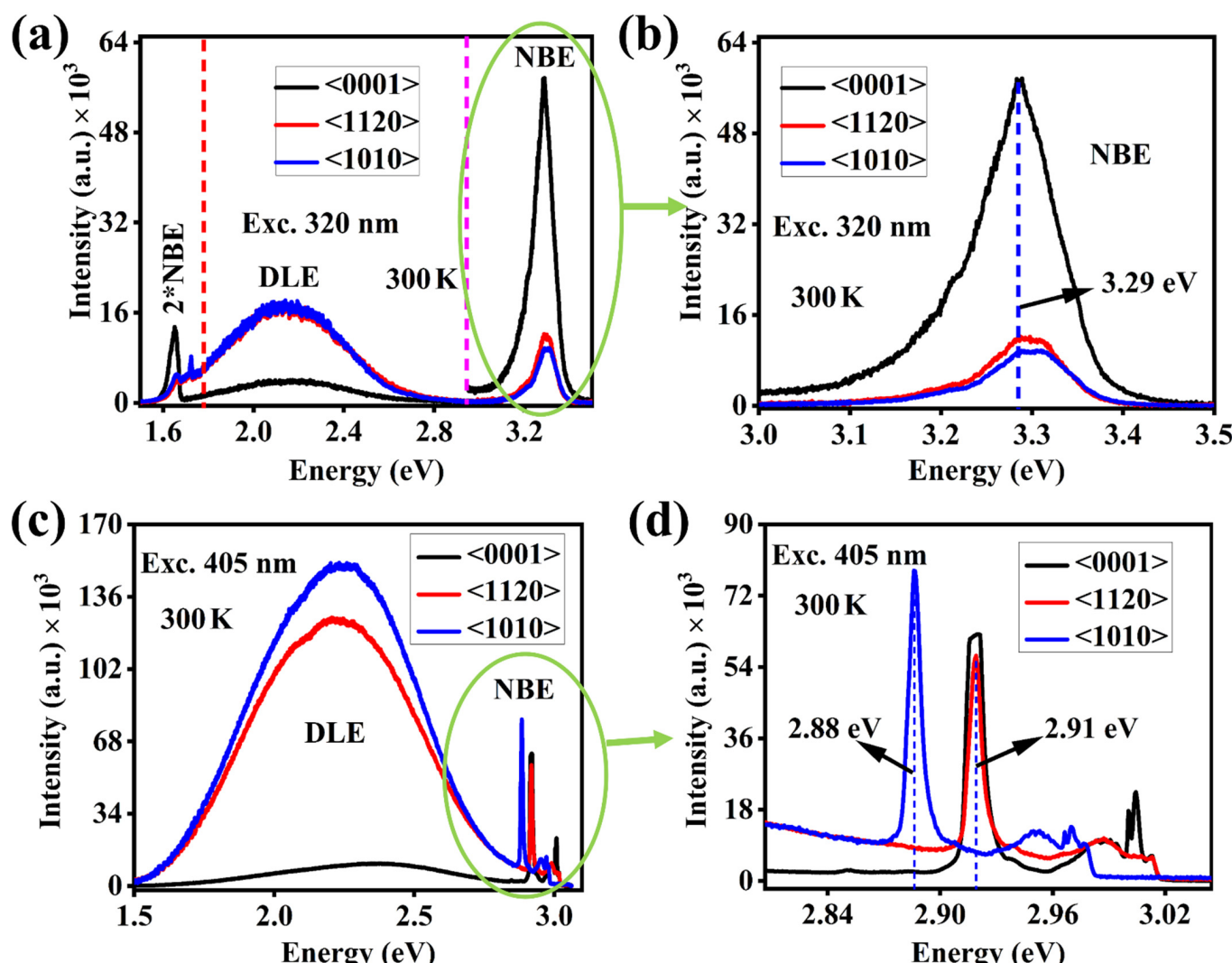


Figure 5. Room-temperature full scan PL spectra of ZnO single crystal with three different orientations (a,b) measured with 320 nm excitation laser, (c,d) measured using 405 nm excitation laser. Here NBE and DLE represents the near-band-edge and deep level emission, respectively.

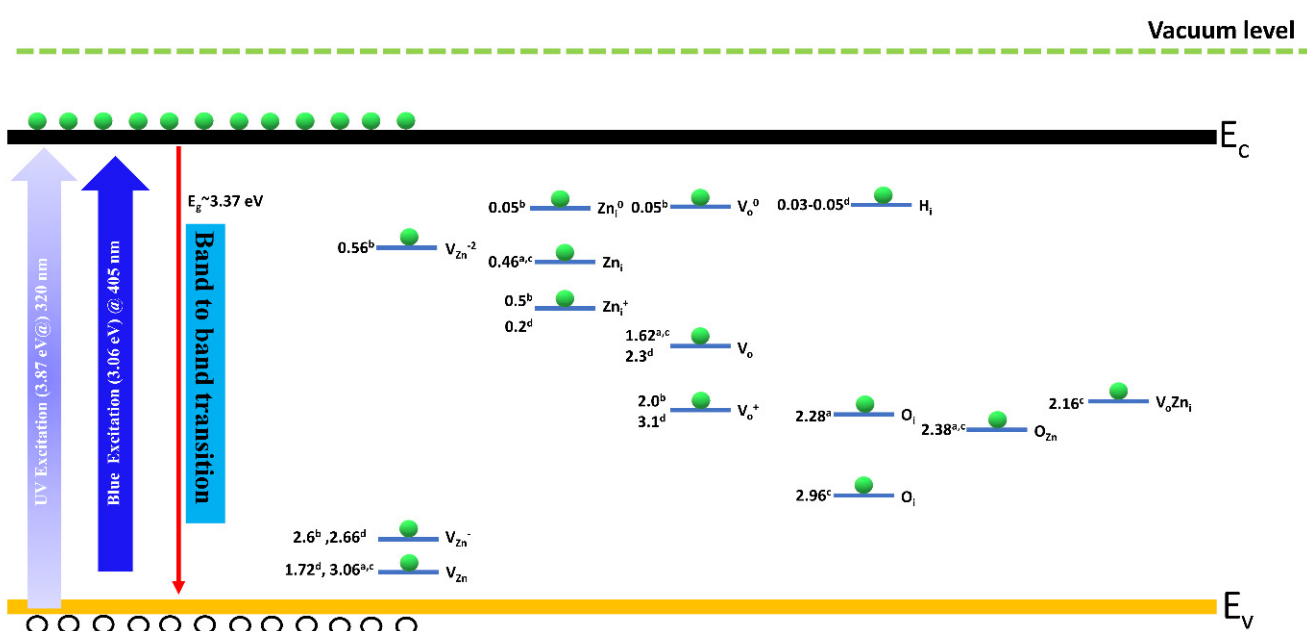


Figure 6. Schematic illustration of energy levels of different possible intrinsic defects in ZnO. The values has been extracted from previous reports: (a) ref. [38] (b) ref. [39] (c) ref. [40] and (d) ref. [41]. The light blue and bluish violet arrow represent the excitation wavelength used in the current study, V_{Zn} , V_{Zn}^- , and V_{Zn}^{-2} indicate the neutral, singly charged, and doubly charged Zn vacancies, respectively. Neutral and singly charged Zn interstitials are denoted by Zn_i , and Zn_i^+ . Neutral and singly charged oxygen vacancies are denoted by V_o , V_o^0 , and V_o^+ . O_i and H_i indicate the oxygen and hydrogen interstitials, respectively. The $V_o Zn_i$ here represents the defect complex containing the oxygen vacancy and Zn interstitial.

Recently, some theoretical studies [34,42,43] suggested that the electronic formation energy of V_o is (0.51 eV) smaller than the formation energy of Zn_i . The V_o formation energy in the orientations $\langle 1120 \rangle$ and $\langle 1010 \rangle$ will most likely be slightly lower than in the orientation $\langle 0001 \rangle$, making it easier to populate these deep levels with more charge carriers. As a result, the DLE region produce more transitions, and the luminescence intensity automatically increases. We also employed a 405 nm excitation laser to measure the PL spectra of ZnO single crystals to investigate the effect of excitation wavelength on emission intensity. As demonstrated in Figure 5c, the 405 nm wavelength stimulated more transitions from the deep levels while emitting negligibly from the near band edge area. This behavior is reasonable since the 405 nm excitation wavelength does not transmit enough energy to activate the electron present in the conduction bands (3.37 eV). However, the transferred energy is enough to excite the deep levels. Furthermore, even with the 405 nm excitation, the $\langle 0001 \rangle$ orientation emits weakly in the DLE area, which indicates that the emission from deep levels depends not only on the excitation wavelength but also on the single crystal orientation, which may be because the deep levels sites present in ZnO single crystals are intrinsic in nature. However, the $\langle 0001 \rangle$ orientation may not be favorable for the presence of these intrinsic defect sites. The NBE region excited with 405 nm wavelength shows the sharp emission at slightly different emission energy (2.91 eV for $\langle 0001 \rangle$ and $\langle 1120 \rangle$ orientation whereas 2.88 eV for $\langle 1010 \rangle$ orientation) plus some background emission in this region (Figure 5d) due to the scattering of an incident photon with the electron presents at the conduction band minima. These peaks could be the 2LO Raman scattering. Figure 2b,d shows a modest blueshift in NBE emission with a higher excitation wavelength, indicating that oxygen vacancies play a significant role in this orientation, since the blueshift without any external doping is attributable to the presence of intrinsic oxygen-related defects [44–46].

For better understanding of different emission centers, present in the NBE region, we have investigated the PL spectra of all three orientations at 123 K, as shown in Figure 7. All three single crystals show five dominant peaks at 3.374, 3.360, 3.346, 3.303, and 3.227 eV, representing the free exciton transition (FX), neutral donor-bound exciton (D^0X) peak, neutral acceptor-bound exciton (A^0X) peak, free electron to acceptor transition (FA) peak, and donor to acceptor pair transition (DAP) peak respectively. However, the $\langle 0001 \rangle$ orientation contains two additional peaks at 3.154 eV and 3.083 eV, which are recognized as the first-order longitudinal optical phonon replica of DAP transition DAP-1LO and DAP-2LO respectively. Conversely, the $\langle 1120 \rangle$ spectra only contain the DAP-1LO peak. The energy separation between these LO phonon replicas was found to be ($\hbar\omega_{LO} = 70\text{--}73\text{ meV}$), consistent with previous reports [47,48]. Semiconductor such as ZnO is well-known for its highly polar nature, making it significant for exciton-phonon coupling. However, the bound excitons are supposed to be the extrinsic transitions that originate from dopants or defects and create discrete energy states for the charge carriers in the bandgap region. In the present case, we used pure ZnO single crystals without any extrinsic dopant, meaning that the transitions from the bound excitons result from intrinsic defects. Based on previous theoretical predictions, these defects could be either V_o or Zn_i [49–51].

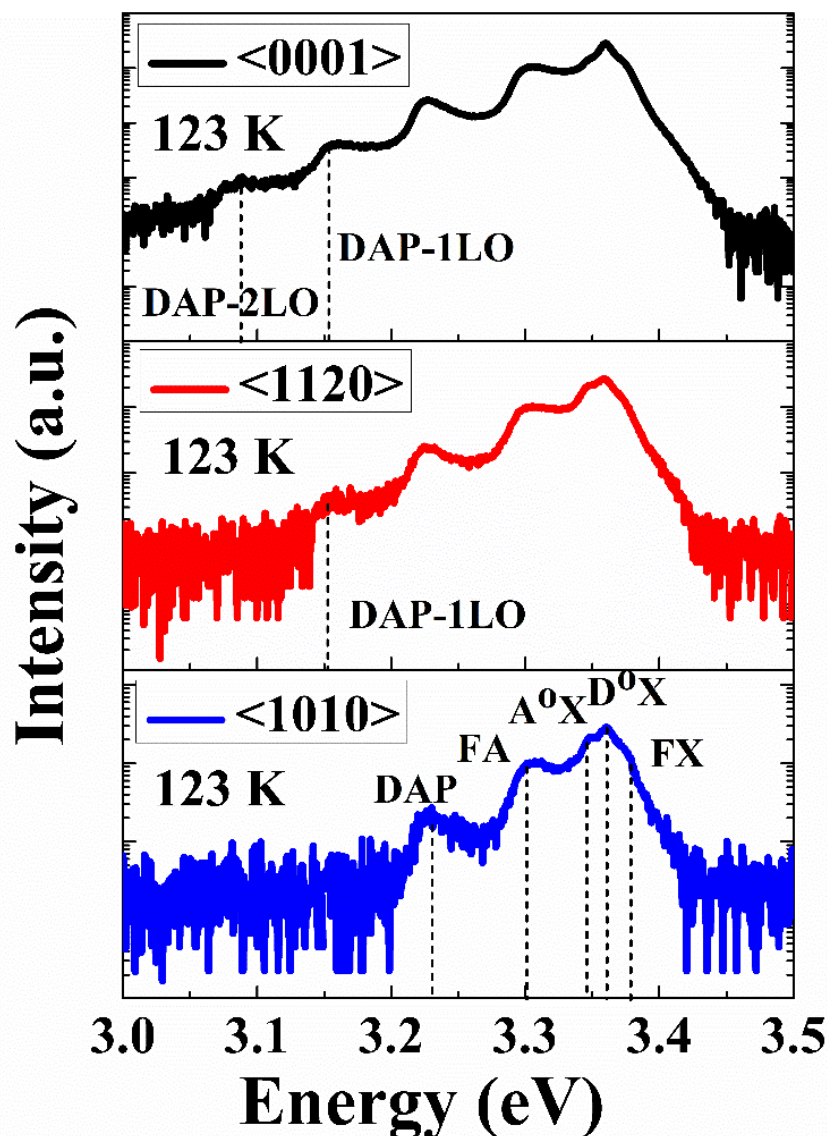


Figure 7. Low-temperature PL spectra of ZnO single crystals having three different orientations.

Figure 8a–c represents the temperature-dependent photoluminescence spectra from cryogenic temperature (123 K) to slight high temperature (543 K) for orientation <0001>, <1120>, and <1010> respectively in the NBE region (3.0–3.5 eV). The PL spectra contain several emission centers, the position and intensity of which varies with the temperature. The neutral donor-bound exciton peak (D^0X) dominates at low temperatures in all three orientations. However, the FX transition becomes more prominent as the temperature increases due to small localization energy [52]. Additionally, the DAP emission shows a redshift with an increase in the temperature. The energy of a photon resulting from the radiative recombination of a DAP transition is given by the following relation,

$$h\nu = E_g - E_A - E_D + q^2/\epsilon r \quad (1)$$

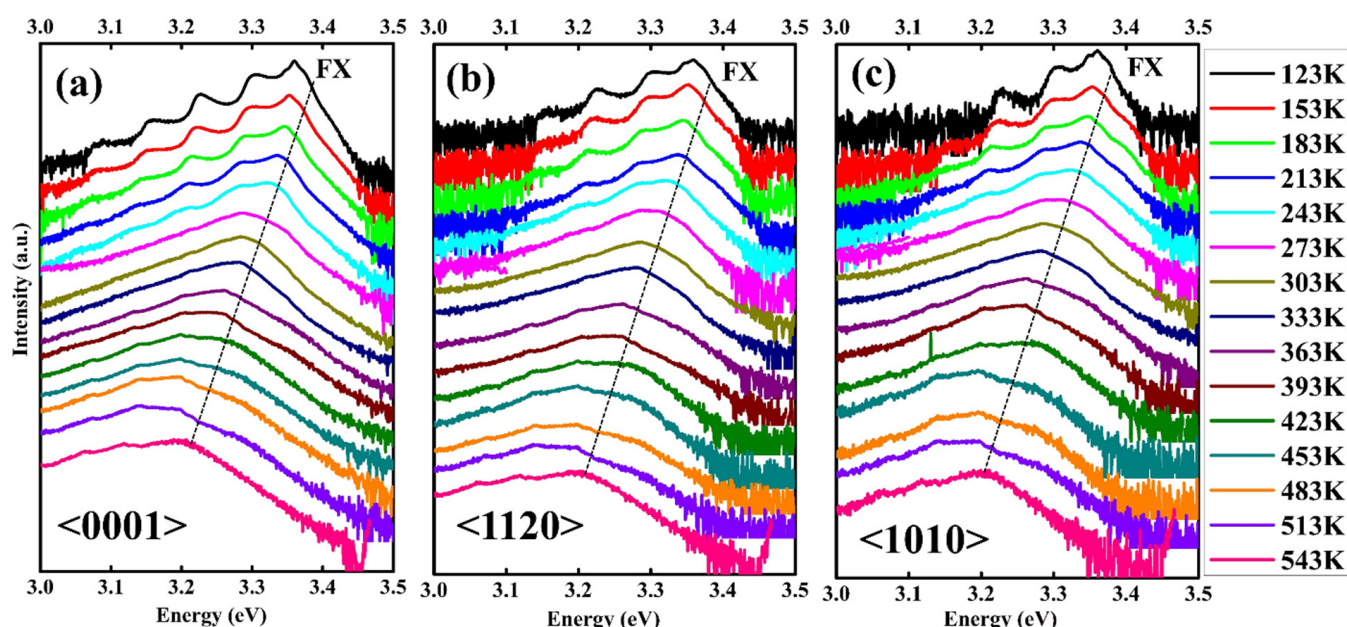


Figure 8. Temperature-dependent near-band-edge emission PL spectra of ZnO Single crystals with (a) <0001> (b) <1120> and (c) <1010> orientation measured over the temperature range 123–543 K using 320 nm excitation laser. The free-exciton (FX) transition dominates at elevated temperature.

Here, E_g represents the bandgap energy, E_A and E_D are acceptor and donor binding energies, respectively, ϵ is the dielectric constant, and “ r ” is the distance between acceptor and donor. While increasing the temperature, the carriers on the DAP site with smaller distance are released into the band and as a result, the line is shifted toward low energy. Moreover, the neutral donor to bound exciton transition (D^0X) shows a blueshift with the increase in temperature since at elevated temperatures; the localized carriers occupy higher energy states after getting thermalized. We analyzed the temperature dependence of FX, D^0X , A^0X , FA, and DAP emission centers for all three single crystals using Varshni's formula, as shown in Figure 9a–c [53]. According to this relation,

$$E_g(T) = E_g(0) - \alpha T^2 / (\beta + T) \quad (2)$$

Here, $E_g(0)$ is the bandgap energy at $T = 0$, T is the absolute temperature whereas α and β are specific constants for ZnO. The obtained values of these constants for three orientation are $E_g(0) \sim 3.37$ eV; $\alpha \sim 1.04, 1.02, 1.09$ meV/K; $\beta \sim 897, 928$, and 1016 K for <0001>, <1120>, and <1010> respectively. Varshni's formula gives the best fit to all the five emission centers for single crystals, and the values obtained in (Table S1) are in good agreement with previous results, except a slight deviation which is negligible as the experimental conditions are not the same as Rai et al. [54] also reported a deviation by a factor of 6 from Giles et al. [55]

where the sample preparation route of both reports is totally different. Therefore, we stated that the slight deviation is ignorable due to the change in experimental conditions [56–58]. Furthermore, in all samples, the peaks represent the linearly decreasing trend, which means that the peak position slightly shifts toward the lower energy with increased temperature, this is quite understandable, as we know that the increase in temperature provides extra energy to the crystal lattice in the form of thermal vibrations, which lowers the binding energies of these charged or neutral pairs presented on these particular sites. As a result, the transition from these sites becomes possible with an excited photon even with slightly less energy. Moreover, the spin-orbit coupling between free exciton and donor to acceptor pair has been found to be 20 meV for polar $<0001>$ and 40 meV for non-polar $<1010>$, and $<1120>$ orientation, which shows a decreasing trend with an increase in temperature. The observed results are in good agreement with previously published reports [59] as the extraction of spin-orbit coupling from the excitonic peak position is quite well-established. There are several studies which theoretically estimated the spin-orbit coupling in ZnO using density functional theory and they reported a value between 16 and 20 meV, for example the work done by Walter et al. [59] which suggested that the value of spin-orbit coupling in ZnO is 20 meV. D.C Look et al. [60] also extracted the spin-orbit coupling for ZnO from PL spectra where they stated that the value is 16 meV. Besides ZnO, Christopher et al. [61] adopted the same strategy to extract the spin-orbit coupling of MoS₂ monolayers just by plotting the peak position over a range of temperature. Considering these all, we think that our adopted technique is a well-established strategy to extract the spin-orbit coupling for our ZnO which even provided the coupling value close to the published literature. Furthermore, the cause of a slight increase in spin-orbit coupling with change in polarity has not been discussed elsewhere. We postulate that it could be the lattice position of Zn atoms in the ZnO crystal lattice, which mediates the coupling between electronic spin and its orbital motion around the nucleus. The electrons of interstitial Zn atoms may face a repulsive interaction with other electrons of neighboring atoms, as the distance between interstitial position and substitutional position is comparatively small. This repulsive force from the surrounding may cause a slight increase in spin-orbit coupling in non-polar ZnO single crystals as they are defect-rich orientations confirmed by XPS and room-temperature photoluminescence analysis.

Figure S1 in Supplementary Materials show the complete scan temperature-dependent PL spectra of ZnO single crystals having three different orientations. Emission centers in the NBE and DLE regions have been found in all orientations with a difference in intensities and full-width half maxima. Moreover, one additional peak (2^*NBE) has also been noted at ~ 1.65 eV, which is a replica of NBE, and it will disappear if we use a long pass filter to capture DLE peak only. The ratio of deep levels emission to the near band edge emission intensity has been calculated for three ZnO single crystals and shown in Table S1 in the Supplementary Materials. It has been noted that the single crystal with orientation $<1010>$ possesses a higher ratio of $I_{\text{DLE}}/I_{\text{NBE}}$ (1.76), and the single crystal with $<0001>$ orientation represents the lowest ratio of (0.04), this indicates that the $<0001>$ orientation contains fewer emission sites in the deep level regions, which means that the crystal grown in this direction is more suitable for UV optical emission. Moreover, it has also been observed that the deep level emission sites are more prevalent in the $<1120>$ and $<1010>$ orientations with decreasing temperature. However, in the $<0001>$ orientation, the effect of these defect-related emission sites is still ignorable even at lower temperatures, and the near band edge emission is still dominant in this orientation. It is likely that, in $<0001>$ orientation, the deep level emission sites lie at higher energy levels indicating that the exciting photon does not have enough energy to activate these luminescent centers (Figure 6) or the ZnO single crystal has significantly less defect densities in this orientation.

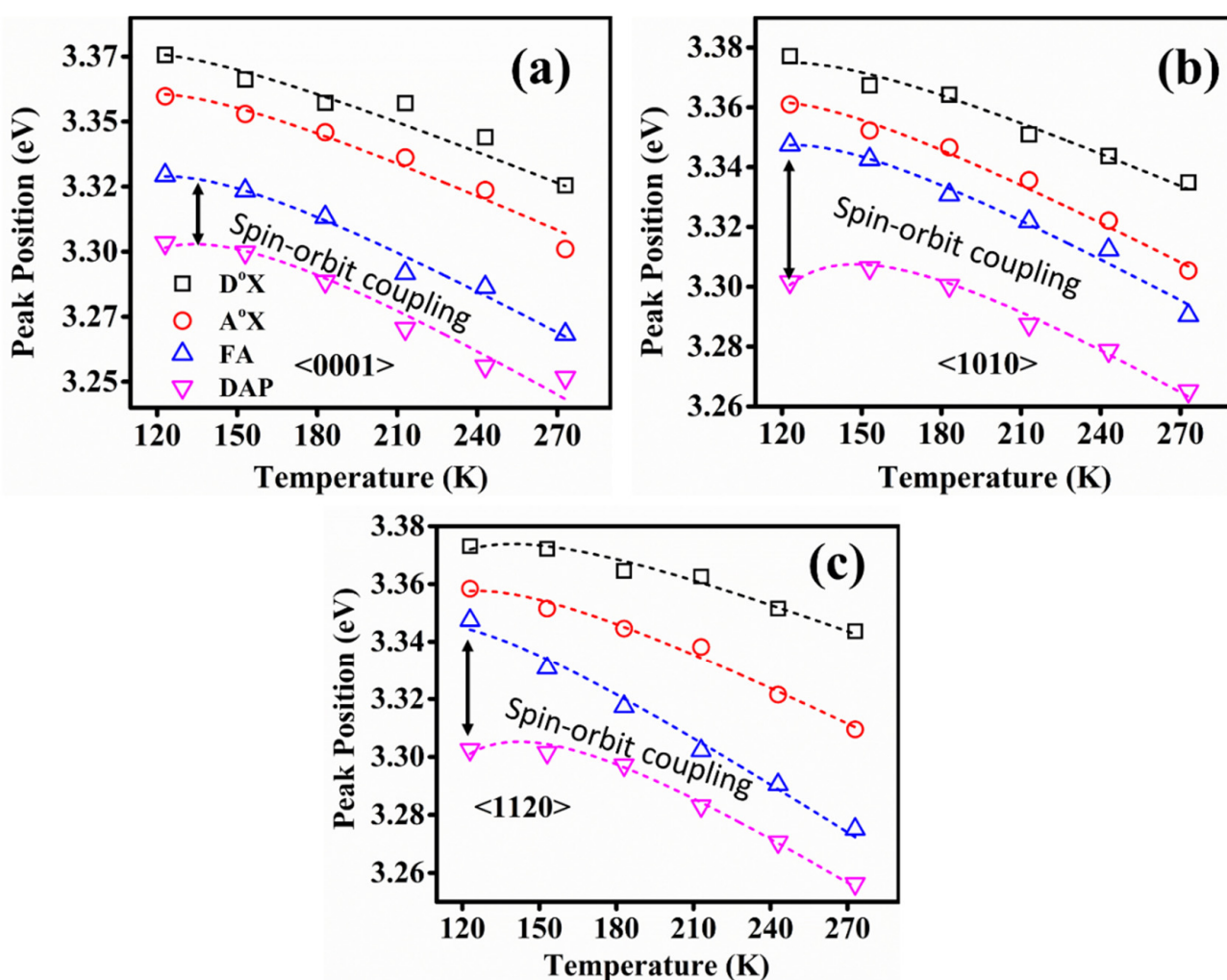


Figure 9. Temperature-dependent variation of peak positions for $D^\circ X$, $A^\circ X$, FA, and DAP transitions of (a) $<0001>$ (b) $<1120>$ and (c) $<1010>$ orientations, respectively. Symbols indicate the experimentally observed peak positions of each transition and dashed lines are the fitting of experimental values with Varshni's empirical formula.

3.5. Excitation-Wavelength-Dependent Photoluminescence Spectroscopy

Figure 10a–c exhibits the excitation power-dependent photoluminescence spectra of ZnO single crystals. We have used the low excitation power of $2.6 \mu\text{W}$ to the highest power of 2.58 mW . It has been noted that the highest photoluminescence in NBE region has been achieved with all orientations using 2.58 mW . As the excitation power decreases, the NBE peaks intensity also decreases whereas the deep level emission dominates at low excitation power, which indicates that the NBE peak intensity has a directly proportional relationship with the excitation power (the relationship of calculated peak position, peak intensity, FWHM, and the ratio of NBE/DLE as a function of excitation power has been elucidated in the Figure S2 in the Supplementary Materials), this is very unpretentious, as the excitation power provides the specific energy to excite the charge carriers present in the valence band. Every electron excited by the incident photon must absorb that specific energy (~equal to the bandgap of that semiconductor material) before transfer to the conduction band. If the excitation power is low, the incident photon will not transfer much energy required to excite the electrons to the conduction band, then there will be no band-to-band transition; however emission from low energy levels or defect sites still has the possibility. Therefore, the emission from DLE dominates at lower excitation power as shown in Figure 10a–c. Similarly, if we use the excitation power that has energy greater

than the bandgap energy of that material, in this case, band-to-band transition will be suppressed due to phonon bottleneck effect. As a result, phonon generation suppresses the electron-hole pair recombination and low NBE emission will be observed. Therefore, it is essential to use the excitation power which can transfer the photon energy equal to the bandgap of that material [62]. Moreover, it has been noted that the same excitation power used for different orientations of ZnO single crystal gives different intensities of luminescence bands present in the ZnO. It means that these luminescence centers are from the intrinsic defect states of ZnO, which does not influence external source. Furthermore, an emission band (at 2.78 eV) emerge in all orientations at low excitation power (0.0026 mW) which is not related to the ZnO sample. We suspect that this emission could be scattering from the system itself as there is no evidence of emission band in ZnO in the literature and it is also not present in other spectra while using higher excitation power. Therefore, we call it “unknown emission” band.

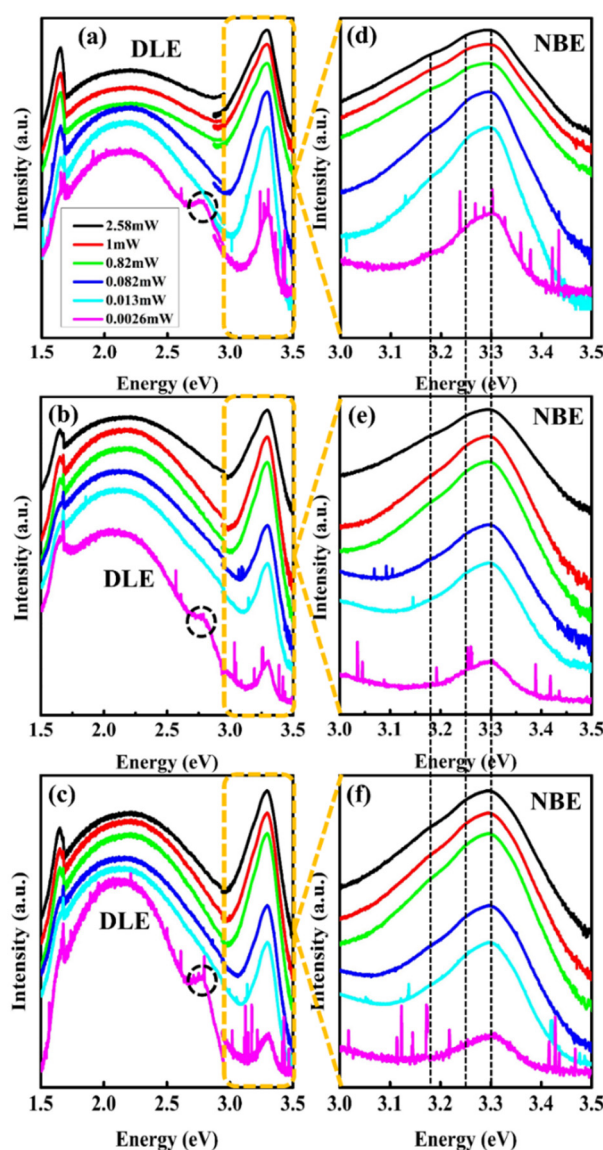


Figure 10. Excitation power-dependent photoluminescence spectra of (a) $<0001>$ (b) $<1120>$ and (c) $<1010>$ orientation of ZnO single crystal. The dashed circle is an “unknown emission band” which is not related to the ZnO but could be scattering from system itself. Figure (d–f) represents the zoom-in on near band edge emission region of $<0001>$, $<1120>$, and $<1010>$ orientation, respectively. Here NBE and DLE represent the near-band-edge and deep level emission, respectively.

Figure 10d–f represents the NBE region of all three orientations. It is well noted that the FX and D⁰X merge after 1 mW excitation power for all orientations. The D⁰X transition becomes dominant at low excitation power. However, as the excitation power increases, more and more DAPs are excited, contributing to the final emission; this happens as a result of the decreased distance between the donor and acceptor, which increases the Coulomb energy in Equation (1) and leads to the higher DAP peak energy. To further evaluate the D⁰X transition characteristics, we depicted the integrated PL intensities of D⁰X for three orientations of ZnO as a function of excitation power measured at room temperature, as shown in Figure 11a. It is worth noting that the PL intensity (I) increases with the excitation power (L), following the below relation,

$$I = \eta L^\alpha \quad (3)$$

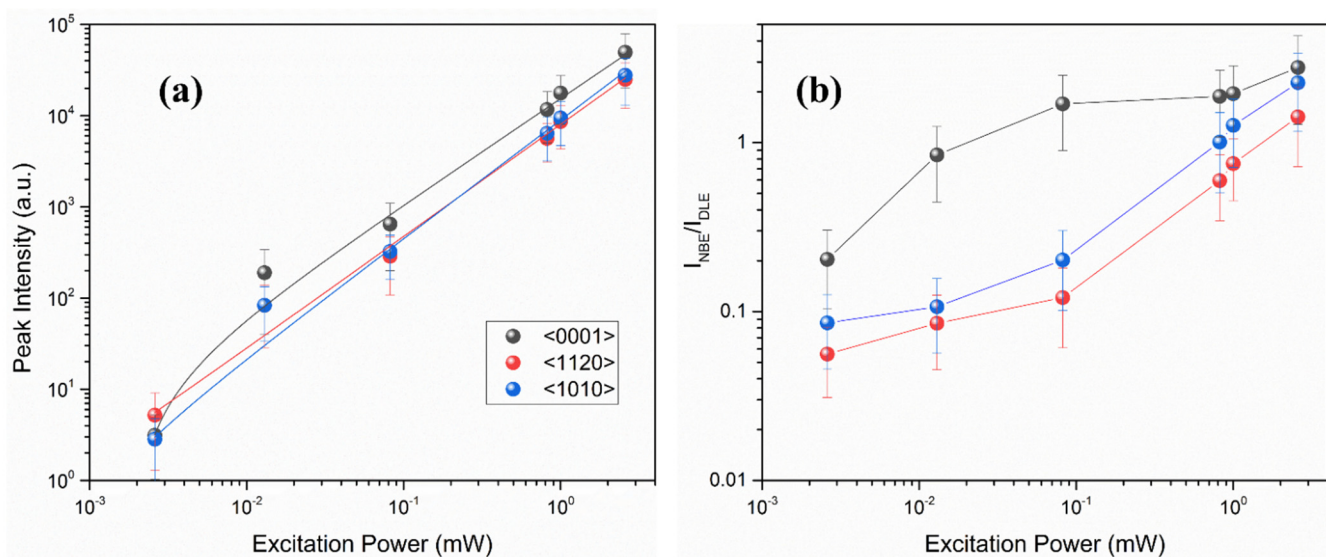


Figure 11. Excitation power-dependent (a) peak intensity of D⁰X, dashed lines are the fitting of experimental data using power law (b) the ratio of near band edge emission intensity to the deep level emission intensity for ZnO single crystal having different orientation. The peak intensity values used here have been extracted from Figure 10 without further processing.

Here, η is the emission efficiency, and α represents the radiative recombination mechanism. For the excitation light having the energy higher than the bandgap energy of the target material, usually $1 < \alpha < 2$ for exciton-like transitions and $\alpha < 1$ for free-to-bound and donor-to-acceptor like transitions [63,64]. The above relation is extensively used as a shred of evidence for finding the origin of the UV emission. In the present work, α has been observed to be 1.148 ± 0.0892 , 1.180 ± 0.0950 , and 1.184 ± 0.0770 for <0001>, <1120>, and <1010> orientations, respectively, which makes it evident that exciton-like transitions are dominant in these samples. A distinct peak appears at 2.78 eV in all three orientations when we used the lowest excitation power (0.0026 mW), while it disappears at other excitation power conditions. This peak is not related to the ZnO samples but rather to the system. Moreover, we have also examined the emission intensity of the NBE peak and DLE peak as a function of excitation power, as shown in Figure 11b. It has been observed that <0001> contains a higher ratio at low excitation power. However, at higher excitation power the difference is not so significant. The trend suggests that the deep levels present in <1120> and <1010> orientations are intrinsic, possibly the oxygen vacancies (V_o). The density of these defects is lower in <0001> orientation, giving rise to a high NBE/DLE ratio even at low excitation power. In short, the current results elucidate that the development of defect-free homoepitaxial substrate for ZnO-based optoelectronic devices, the <0001> orientation will be much beneficial as the fraction of intrinsic oxygen-related defects is less.

Furthermore, the free-excitonic transitions are dominant at higher temperatures in ZnO which can be helpful in the fabrication of ZnO-based UV diodes.

4. Conclusions

A detailed investigation of temperature-dependent, excitation power-dependent, and orientation-mediated photoluminescence of ZnO single crystals has been carried out systematically. The room-temperature PL spectra of ZnO single crystal with different excitation wavelengths indicate that the excitation wavelength comparable to or slightly below the bandgap energy, causing more transition in near band edge area with less deep level transition indicating that the choice of excitation wavelength can suppress the emission from deep levels which is required to fabricate ZnO-based high-efficient UV diodes. However, even utilizing the same excitation wavelength, the orientation of a single crystal is equally critical for achieving intense NBE emission. In our case, we discovered that the $<0001>$ orientation is better in terms of high emission in NBE with low DLE emission which is required for the development of homoepitaxial substrate for ZnO-based optoelectronic devices. The temperature-dependent PL measurements show multiple emission centers contributing to the near band edge emission region with dominant behavior of D^0X transition in all samples at low temperature (123 K). The FX transition became more obvious as the temperature increased (543 K), indicating the free-excitonic transitions are dominant at higher temperature in ZnO, which can be helpful in fabricating ZnO-based UV diodes. The excitation power-dependent Photoluminescence results suggest that the $<0001>$ orientation is more suitable for high excitonic emission with dominant D^0X transition. Furthermore, we discovered that oxygen vacancies are the primary source of deep level emission in ZnO, and the larger densities of these inherent defects are present in $<1120>$ and $<1010>$ orientations. Therefore, the current study proposed that the use of $<0001>$ ZnO single crystal can solve the problem of lattice mismatch and ionic diffusion offered by the heteroepitaxial substrate. Furthermore, the heat mismatching or phonon generation can also be suppressed by utilizing $<0001>$ single crystal as a homoepitaxial substrate for ZnO-based optoelectronic devices.

Supplementary Materials: The following supporting information can be downloaded at: <https://www.mdpi.com/article/10.3390/nano12132192/s1>, Figure S1: Complete scan of temperature-dependent photoluminescence spectra of (a) $<0001>$ (b) $<1120>$ (c) $<1010>$ orientation of ZnO single crystals measured with an excitation wavelength of 320 nm from the temperature range 123–543 K. Figure S2: For ZnO single crystals with three distinct orientations, the relationship between (a) peak intensity (b) peak position (c) FWHM (d) ratio of NBE/DLE intensity as a function of excitation power is shown. The dashed lines represent a linear fit of the experimentally observed data points, while the symbols represent experimentally observed data. Table S1: Room-temperature PL peaks position, intensity ratio, and the Varshni's fit parameters for ZnO single crystals with different orientations.

Author Contributions: Conceptualization, investigation, and writing—original draft preparation, A.H. and A.A.K.; writing—review and editing, M.A., M.Z., A.A.K., W.X., and Y.H.A.; funding acquisition, A.A.K., Y.C., and Y.H.A. All authors have read and agreed to the published version of the manuscript.

Funding: This work was supported by the Basic Science Research Program (2021R1A6A1A10044950) and the Midcareer Researcher Program (2020R1A2C1005735) through a National Research Foundation grant funded by the Korea Government and by the Zhejiang Provincial Natural Science Foundation of China under Grant No. (LZ20E050003).

Data Availability Statement: The data are contained within the article or Supplementary Materials.

Conflicts of Interest: The authors declare no conflict of interest.

References

1. Liu, Y.; Dong, J.; Hesketh, P.J.; Liu, M. Synthesis and gas sensing properties of ZnO single crystal flakes. *J. Mater. Chem.* **2005**, *15*, 2316–2320. [[CrossRef](#)]
2. Wu, T.; Deng, G.; Zhen, C. Metal oxide mesocrystals and mesoporous single crystals: Synthesis, properties and applications in solar energy conversion. *J. Mater. Sci. Technol.* **2021**, *73*, 9–22. [[CrossRef](#)]
3. Dworschak, D.; Brunnhofer, C.; Valtiner, M. Photocorrosion of ZnO Single Crystals during Electrochemical Water Splitting. *ACS Appl. Mater. Interfaces* **2020**, *12*, 51530–51536. [[CrossRef](#)] [[PubMed](#)]
4. Tishkevich, D.I.; Grabchikov, S.S.; Tsybulskaya, L.S.; Shendyukov, V.S.; Perevoznikov, S.S.; Trukhanov, S.V.; Trukhanova, E.L.; Trukhanov, A.V.; Vinnik, D.A. Electrochemical deposition regimes and critical influence of organic additives on the structure of Bi films. *J. Alloys Compd.* **2018**, *735*, 1943–1948. [[CrossRef](#)]
5. Mukhanov, V.A.; Sokolov, P.S.; Baranov, A.N.; Timoshenko, V.Y.; Zhigunov, D.M.; Solozhenko, V.L. Congruent melting and rapid single-crystal growth of ZnO at 4 GPa. *CrystEngComm* **2013**, *15*, 6318–6322. [[CrossRef](#)]
6. Lin, W.; Ding, K.; Lin, Z.; Zhang, J.; Huang, J.; Huang, F. The growth and investigation on Ga-doped ZnO single crystals with high thermal stability and high carrier mobility. *CrystEngComm* **2011**, *13*, 3338–3341. [[CrossRef](#)]
7. Tishkevich, D.I.; Vorobjova, A.I.; Vinnik, D. Formation and Corrosion Behavior of Nickel/Alumina Nanocomposites. *Solid State Phenom.* **2020**, *299*, 100–106. [[CrossRef](#)]
8. Li, Z.; Jiang, M.; Sun, Y.; Zhang, Z.; Li, B.; Zhao, H.; Shan, C.; Shen, D. Electrically pumped Fabry–Perot microlasers from single Ga-doped ZnO microbelt based heterostructure diodes. *Nanoscale* **2018**, *10*, 18774–18785. [[CrossRef](#)]
9. Liu, W.Z.; Xu, H.Y.; Wang, C.L.; Zhang, L.X.; Zhang, C.; Sun, S.Y.; Ma, J.G.; Zhang, X.T.; Wang, J.N.; Liu, Y.C. Enhanced ultraviolet emission and improved spatial distribution uniformity of ZnO nanorod array light-emitting diodes via Ag nanoparticles decoration. *Nanoscale* **2013**, *5*, 8634–8639. [[CrossRef](#)]
10. Chen, D.; Xin, Y.; Lu, B.; Pan, X.; Huang, J.; He, H.; Ye, Z. Self-powered ultraviolet photovoltaic photodetector based on graphene/ZnO heterostructure. *Appl. Surf. Sci.* **2020**, *529*, 147087. [[CrossRef](#)]
11. Nicholas, N.J.; Ducker, W.; Franks, G.V. Differential Etching of ZnO Native Planes under Basic Conditions. *Langmuir* **2012**, *28*, 5633–5641. [[CrossRef](#)] [[PubMed](#)]
12. Yatskiv, R.; Grym, J.; Tiagulskyi, S.; Bašinová, N. Influence of Surface Polarity on Optoelectronic Properties of PEDOT:PSS/ZnO Hybrid Heterojunctions. *Phys. Status Solidi (a)* **2021**, *218*, 2000612. [[CrossRef](#)]
13. Sasaki, H.; Kato, H.; Izumida, F.; Endo, H.; Maeda, K.; Ikeda, M.; Kashiwaba, Y.; Niikura, I.; Kashiwaba, Y. Photoluminescence properties of ZnO single crystals with polar and non-polar faces. *Phys. Status Solidi (c)* **2006**, *3*, 1034–1037. [[CrossRef](#)]
14. Meyer, B.K.; Alves, H.; Hofmann, D.M.; Kriegseis, W.; Forster, D.; Bertram, F.; Christen, J.; Hoffmann, A.; Straßburg, M.; Dworzak, M.; et al. Bound exciton and donor–acceptor pair recombinations in ZnO. *Phys. Status Solidi (b)* **2004**, *241*, 231–260. [[CrossRef](#)]
15. Ohashi, N.; Ishigaki, T.; Okada, N.; Taguchi, H.; Sakaguchi, I.; Hishita, S.; Sekiguchi, T.; Haneda, H. Passivation of active recombination centers in ZnO by hydrogen doping. *J. Appl. Phys.* **2003**, *93*, 6386–6392. [[CrossRef](#)]
16. Yang, L.L.; Zhao, Q.X.; Willander, M.; Liu, X.J.; Fahlman, M.; Yang, J.H. Origin of the surface recombination centers in ZnO nanorods arrays by X-ray photoelectron spectroscopy. *Appl. Surf. Sci.* **2010**, *256*, 3592–3597. [[CrossRef](#)]
17. Son, N.T.; Ivanov, I.G.; Kuznetsov, A.; Svensson, B.G.; Zhao, Q.X.; Willander, M.; Morishita, N.; Ohshima, T.; Itoh, H.; Isoya, J.; et al. Recombination centers in as-grown and electron-irradiated ZnO substrates. *J. Appl. Phys.* **2007**, *102*, 093504. [[CrossRef](#)]
18. Cole, J.J.; Wang, X.; Knuesel, R.J.; Jacobs, H.O. Integration of ZnO Microcrystals with Tailored Dimensions Forming Light Emitting Diodes and UV Photovoltaic Cells. *Nano Lett.* **2008**, *8*, 1477–1481. [[CrossRef](#)] [[PubMed](#)]
19. Wang, M.; Zhang, L. The influence of orientation on the photoluminescence behavior of ZnO thin films obtained by chemical solution deposition. *Mater. Lett.* **2009**, *63*, 301–303. [[CrossRef](#)]
20. Marin, O.; Tirado, M.; Budini, N.; Mosquera, E.; Figueroa, C.; Comedi, D. Photoluminescence from c-axis oriented ZnO films synthesized by sol-gel with diethanolamine as chelating agent. *Mater. Sci. Semicond. Process.* **2016**, *56*, 59–65. [[CrossRef](#)]
21. Kalyanaraman, S.; Vettumperumal, R.; Thangavel, R. Study of multiple phonon behavior in Li-doped ZnO thin films fabricated using the sol-gel spin-coating technique. *J. Korean Phys. Soc.* **2013**, *62*, 804–808. [[CrossRef](#)]
22. Cuscó, R.; Alarcón-Lladó, E.; Ibáñez, J.; Artús, L.; Jiménez, J.; Wang, B.; Callahan, M.J. Temperature dependence of Raman scattering in ZnO. *Phys. Rev. B* **2007**, *75*, 165202. [[CrossRef](#)]
23. Ashkenov, N.; Mbenkum, B.N.; Bundesmann, C.; Riede, V.; Lorenz, M.; Spemann, D.; Kaidashev, E.M.; Kasic, A.; Schubert, M.; Grundmann, M.; et al. Infrared dielectric functions and phonon modes of high-quality ZnO films. *J. Appl. Phys.* **2002**, *93*, 126–133. [[CrossRef](#)]
24. Giri, P.K.; Bhattacharyya, S.; Singh, D.K.; Kesavamoorthy, R.; Panigrahi, B.K.; Nair, K.G.M. Correlation between microstructure and optical properties of ZnO nanoparticles synthesized by ball milling. *J. Appl. Phys.* **2007**, *102*, 093515. [[CrossRef](#)]
25. Lima, L.; Caldas, L.D.S.; Alí, A.; Barreto, J.; Freitas, R.; Mazzarella, A.; Felix, G.; Carozo, V.; Stavale, F. Growth and Raman spectroscopy of ultrathin ZnO(0001) films on Ag(001). *Surf. Sci.* **2021**, *704*, 121748. [[CrossRef](#)]
26. Calleja, J.M.; Cardona, M. Resonant Raman scattering in ZnO. *Phys. Rev. B* **1977**, *16*, 3753–3761. [[CrossRef](#)]
27. Satyarthi, P.; Ghosh, S.; Mishra, P.; Sekhar, B.R.; Singh, F.; Kumar, P.; Kanjilal, D.; Dhaka, R.S.; Srivastava, P. Defect controlled ferromagnetism in xenon ion irradiated zinc oxide. *J. Magn. Magn. Mater.* **2015**, *385*, 318–325. [[CrossRef](#)]

28. Al-Gaashani, R.; Radiman, S.; Daud, A.R.; Tabet, N.; Al-Douri, Y. XPS and optical studies of different morphologies of ZnO nanostructures prepared by microwave methods. *Ceram. Int.* **2013**, *39*, 2283–2292. [[CrossRef](#)]
29. Tay, Y.Y.; Tan, T.T.; Liang, M.H.; Boey, F.; Li, S. Specific defects, surface band bending and characteristic green emissions of ZnO. *Phys. Chem. Chem. Phys.* **2010**, *12*, 6008–6013. [[CrossRef](#)] [[PubMed](#)]
30. Chen, M.; Wang, X.; Yu, Y.H.; Pei, Z.L.; Bai, X.D.; Sun, C.; Huang, R.F.; Wen, L.S. X-ray photoelectron spectroscopy and auger electron spectroscopy studies of Al-doped ZnO films. *Appl. Surf. Sci.* **2000**, *158*, 134–140. [[CrossRef](#)]
31. Pandey, B.; Ghosh, S.; Srivastava, P.; Kumar, P.; Kanjilal, D. Influence of microstructure on room temperature ferromagnetism in Ni implanted nanodimensional ZnO films. *J. Appl. Phys.* **2009**, *105*, 033909. [[CrossRef](#)]
32. Hassan, A.; Jin, Y.; Irfan, M.; Jiang, Y. Acceptor-modulated optical enhancements and band-gap narrowing in ZnO thin films. *AIP Adv.* **2018**, *8*, 035212. [[CrossRef](#)]
33. Fang, Z.B.; Yan, Z.J.; Tan, Y.S.; Liu, X.Q.; Wang, Y.Y. Influence of post-annealing treatment on the structure properties of ZnO films. *Appl. Surf. Sci.* **2005**, *241*, 303–308. [[CrossRef](#)]
34. Clark, S.J.; Robertson, J.; Lany, S.; Zunger, A. Intrinsic defects in ZnO calculated by screened exchange and hybrid density functionals. *Phys. Rev. B* **2010**, *81*, 115311. [[CrossRef](#)]
35. Vidya, R.; Ravindran, P.; Fjellvåg, H.; Svensson, B.G.; Monakhov, E.; Ganchenkova, M.; Nieminen, R.M. Energetics of intrinsic defects and their complexes in ZnO investigated by density functional calculations. *Phys. Rev. B* **2011**, *83*, 045206. [[CrossRef](#)]
36. Cui, M.; Zhang, Z.; Wang, Y.; Finch, A.; Townsend, P.D. Temperature dependence of bulk luminescence from ZnO. *Luminescence* **2018**, *33*, 654–659. [[CrossRef](#)] [[PubMed](#)]
37. Janotti, A.; Van de Walle, C.G. Oxygen vacancies in ZnO. *Appl. Phys. Lett.* **2005**, *87*, 122102. [[CrossRef](#)]
38. Lin, B.; Fu, Z.; Jia, Y. Green luminescent center in undoped zinc oxide films deposited on silicon substrates. *Appl. Phys. Lett.* **2001**, *79*, 943–945. [[CrossRef](#)]
39. Lima, S.A.M.; Sigoli, F.A.; Jafelicci Jr, M.; Davolos, M.R. Luminescent properties and lattice defects correlation on zinc oxide. *Int. J. Inorg. Mater.* **2001**, *3*, 749–754. [[CrossRef](#)]
40. Xu, P.S.; Sun, Y.M.; Shi, C.S.; Xu, F.Q.; Pan, H.B. The electronic structure and spectral properties of ZnO and its defects. *Nucl. Instrum. Methods Phys. Res. Sect. B: Beam Interact. Mater. At.* **2003**, *199*, 286–290. [[CrossRef](#)]
41. Nickel, N.H.; Terukov, E. Zinc Oxide—A Material for Micro-and Optoelectronic Applications. In Proceedings of the NATO Advanced Research Workshop on Zinc Oxide as a Material for Micro-and Optoelectronic Applications, Saint Petersburg, Russia, 23–25 June 2004; Springer Science & Business Media: Dordrecht, The Netherland, 2006; Volume 194.
42. Oba, F.; Togo, A.; Tanaka, I.; Paier, J.; Kresse, G. Defect energetics in ZnO: A hybrid Hartree-Fock density functional study. *Phys. Rev. B* **2008**, *77*, 245202. [[CrossRef](#)]
43. Bjørheim, T.S.; Kotomin, E. Ab Initio Thermodynamics of Oxygen Vacancies and Zinc Interstitials in ZnO. *J. Phys. Chem. Lett.* **2014**, *5*, 4238–4242. [[CrossRef](#)] [[PubMed](#)]
44. van Sark, W.G.J.H.M.; Frederix, P.L.T.M.; Bol, A.A.; Gerritsen, H.C.; Meijerink, A. Blueing, Bleaching, and Blinking of Single CdSe/ZnS Quantum Dots. *ChemPhysChem* **2002**, *3*, 871–879. [[CrossRef](#)]
45. Derfus, A.M.; Chan, W.C.W.; Bhatia, S.N. Probing the Cytotoxicity of Semiconductor Quantum Dots. *Nano Lett.* **2004**, *4*, 11–18. [[CrossRef](#)]
46. Ozasa, K.; Nemoto, S.; Maeda, M.; Hara, M. Excitation-wavelength-dependent photoluminescence evolution of CdSe/ZnS nanoparticles. *J. Appl. Phys.* **2007**, *101*, 103503. [[CrossRef](#)]
47. Zhang, X.T.; Liu, Y.C.; Zhi, Z.Z.; Zhang, J.Y.; Lu, Y.M.; Shen, D.Z.; Xu, W.; Fan, X.W.; Kong, X.G. Temperature dependence of excitonic luminescence from nanocrystalline ZnO films. *J. Lumin.* **2002**, *99*, 149–154. [[CrossRef](#)]
48. Li, T.; Zhu, Y.; Ji, X.; Zheng, W.; Lin, Z.; Lu, X.; Huang, F. Experimental Evidence on Stability of N Substitution for O in ZnO Lattice. *J. Phys. Chem. Lett.* **2020**, *11*, 8901–8907. [[CrossRef](#)]
49. Huang, G.-Y.; Wang, C.-Y.; Wang, J.-T. First-principles study of diffusion of oxygen vacancies and interstitials in ZnO. *J. Phys.: Condens. Matter* **2009**, *21*, 195403. [[CrossRef](#)]
50. Li, H.; Schirra, L.K.; Shim, J.; Cheun, H.; Kippelen, B.; Monti, O.L.A.; Bredas, J.-L. Zinc Oxide as a Model Transparent Conducting Oxide: A Theoretical and Experimental Study of the Impact of Hydroxylation, Vacancies, Interstitials, and Extrinsic Doping on the Electronic Properties of the Polar ZnO (0002) Surface. *Chem. Mater.* **2012**, *24*, 3044–3055. [[CrossRef](#)]
51. Zhang, M.; Averseng, F.; Krafft, J.-M.; Borghetti, P.; Costentin, G.; Stankic, S. Controlled Formation of Native Defects in Ultrapure ZnO for the Assignment of Green Emissions to Oxygen Vacancies. *J. Phys. Chem. C* **2020**, *124*, 12696–12704. [[CrossRef](#)]
52. Wu, K.; He, H.; Lu, Y.; Huang, J.; Ye, Z. Dominant free exciton emission in ZnO nanorods. *Nanoscale* **2012**, *4*, 1701–1706. [[CrossRef](#)] [[PubMed](#)]
53. Varshni, Y.P. Temperature dependence of the energy gap in semiconductors. *Physica* **1967**, *34*, 149–154. [[CrossRef](#)]
54. Rai, R.C.; Gumiñak, M.; Wilser, S.; Cai, B.; Nakarmi, M.L. Elevated temperature dependence of energy band gap of ZnO thin films grown by e-beam deposition. *J. Appl. Phys.* **2012**, *111*, 073511. [[CrossRef](#)]
55. Wang, L.; Giles, N.C. Temperature dependence of the free-exciton transition energy in zinc oxide by photoluminescence excitation spectroscopy. *J. Appl. Phys.* **2003**, *94*, 973–978. [[CrossRef](#)]
56. Lee, S.H.; Lee, J.S.; Ko, W.B.; Sohn, J.I.; Cha, S.N.; Kim, J.M.; Park, Y.J.; Hong, J.P. Photoluminescence Analysis of Energy Level on Li-Doped ZnO Nanowires Grown by a Hydrothermal Method. *Appl. Phys. Express* **2012**, *5*, 095002. [[CrossRef](#)]

57. Zhang, Y.; Lin, B.; Sun, X.; Fu, Z. Temperature-dependent photoluminescence of nanocrystalline ZnO thin films grown on Si (100) substrates by the sol–gel process. *Appl. Phys. Lett.* **2005**, *86*, 131910. [[CrossRef](#)]
58. Fonoberov, V.A.; Alim, K.A.; Balandin, A.A.; Xiu, F.; Liu, J. Photoluminescence investigation of the carrier recombination processes in ZnO quantum dots and nanocrystals. *Phys. Rev. B* **2006**, *73*, 165317. [[CrossRef](#)]
59. Lambrecht, W.R.L.; Rodina, A.V.; Limpijumnong, S.; Segall, B.; Meyer, B.K. Valence-band ordering and magneto-optic exciton fine structure in ZnO. *Phys. Rev. B* **2002**, *65*, 075207. [[CrossRef](#)]
60. Reynolds, D.C.; Look, D.C.; Jogai, B.; Litton, C.W.; Cantwell, G.; Harsch, W.C. Valence-band ordering in ZnO. *Phys. Rev. B* **1999**, *60*, 2340–2344. [[CrossRef](#)]
61. Christopher, J.W.; Goldberg, B.B.; Swan, A.K. Long tailed trions in monolayer MoS₂: Temperature dependent asymmetry and resulting red-shift of trion photoluminescence spectra. *Sci. Rep.* **2017**, *7*, 14062. [[CrossRef](#)]
62. Cui, J.B.; Thomas, M.A. Power dependent photoluminescence of ZnO. *J. Appl. Phys.* **2009**, *106*, 033518. [[CrossRef](#)]
63. Schmidt, T.; Lischka, K.; Zulehner, W. Excitation-power dependence of the near-band-edge photoluminescence of semiconductors. *Phys. Rev. B* **1992**, *45*, 8989–8994. [[CrossRef](#)] [[PubMed](#)]
64. Kurbanov, S.; Igamberdiev, K.; Yuldashev, S.; Kang, T.W. Excitation Intensity Dependent Studies of Photoluminescence from ZnO Nanocrystals Deposited on Different Substrates. *Jpn. J. Appl. Phys.* **2009**, *48*, 115004. [[CrossRef](#)]